ELECTROCHEMISTRY

Tunable CO/H_2 ratios of electrochemical reduction of CO_2 through the Zn-Ln dual atomic catalysts

Zhong Liang[1], Lianpeng Song[1], Mingzi Sun[2], Bolong Huang[2]*, Yaping Du[1]*

Electrochemical reduction of CO_2 (CO_2RR) to value-added liquid fuels is a highly appealing solution for carbon-neutral recycling, especially to syngas (CO/H_2). Current strategies suffer from poor faradaic efficiency (FE), selectivity, and controllability to the ratio of products. In this work, we have synthesized a series of single and dual atomic catalysts on the carbon nitride nanosheets. Adjusting the ratio of La and Zn atomic sites produces syngas with a wide range of CO/H_2 ratios. Moreover, the ZnLa-1/CN electrocatalyst generates the syngas with a ratio of CO/H_2 = 0.5 at a wide potential range, and the total FE of CO2RR reaches 80% with good stability. Density functional theory calculations have confirmed that the Zn and La affect electronic structures and determine the formation of CO and H_2, respectively. This work indicates a promising strategy in the development of atomic catalysts for more controllable CO_2RR.

INTRODUCTION

The massive consumption of fossil fuels has led to a continuous increase in carbon dioxide (CO_2) emissions. Many environmental issues caused by the emission of CO_2 including the greenhouse effect have received more and more attention all over the world (*1*–*5*). Meanwhile, the rapid consumption of fossil energy leads to a severe energy crisis. In this regard, many emerging technologies have been proposed, such as sequestration, chemical fixation, and electro/photochemical reduction, to inhibit CO_2 release. Reduction of CO_2 through the electrochemical method (eCRR) as a promising solution to reduce the concentration of CO_2 in the atmosphere has attracted lots of researchers' attention (*6*–*11*). Meanwhile, the value-added liquid fuels and chemical feedstocks obtained from the eCRR process can also meet the energy requirement to some extent in the future. However, high overpotential is required to activate CO_2 because of the high stability of CO_2 molecules. At the same time, hydrogen evolution reaction (HER) is the main competitive process during eCRR, making the faradaic efficiency (FE) and selectivity of eCRR still very low (*12*). Although major efforts have been made on suppressing HER and activating CO_2 molecules, such as designing various electrocatalysts, electrodes, or cell structures, catalysts with high FE and selectivity and low price are also urgently demanded.

Rather than prohibiting the HER process, combining eCRR and HER to synthesis syngas with tunable CO/H_2 ratio is a good alternative (*13*–*18*). The CO/H_2 ratio in the syngas is of great significance for meeting the requirements for specific products: CO/H_2 = 1:2 for methanol synthesis and Fischer-Tropsch reactions, CO/H_2 = 1:1-3.33 for syngas fermentation, and CO/H_2 = 1:1 for dimethyl ether (*15*, *19*, *20*). This is especially attractive because the direct eCRR to methanol or other liquid products currently has a relatively low FE and selectivity, and the separation of final products is also very difficult. Therefore, it is necessary to develop electrocatalysts that can produce a suitable CO/H_2 ratio with high syngas yield. Currently, Cu is the only element reported that can produce hydrocarbons through eCRR. Other elements, like gold (Au), silver (Ag), zinc (Zn), and palladium (Pd), have been widely investigated for CO production (*21*). Among these materials, Zn has a lower price and relatively high selectivity for CO. Rare earth (RE) elements including yttrium (Y), scandium (Sc), and lanthanide elements play important roles in many fields because of their special electronic structure (*22*–*26*).

Single atom catalysts have received increasing attention because of their high atomic utilization efficiency and excellent catalytic activity or selectivity. In reactions including HER, oxygen evolution reaction, oxygen reduction reaction, nitrogen reduction reaction, and eCRR, single atom catalysts show low overpotentials, high current density, or excellent stability (*27*–*32*). For the electrochemical CO_2 reduction process, single atom catalysts of Ni, Co, Fe, Mn, Bi, Pd, and Zn prefer to produce CO in CO_2 saturated electrolytes (*21*). At the same time, single Cu atom catalysts can generate various products through the reduction of CO_2. Sn, Mo, and In single atom catalysts prefer to generate formic acid during this process (*21*). In addition, the unique structural properties of RE elements at the single atom scale may endow them with unexpected performance that nanoscale and microscale materials do not own. Moreover, when atomic pairs are formed between different atoms, the interactions between the electronic structures might make it possible for the adsorption and desorption of the reaction intermediate to reach a suitable state. Therefore, dual atomic catalysts may show superior activity, higher selectivity, or stability than corresponding single atomic catalysts (*33*–*38*). Also, the combination of transition metal–based single atom and single atomic RE may have unexpected effects on eCRR. In this work, the ratio of CO and H_2 in syngas was tuned by adjusting the amount of Zn and lanthanum (La) centers, and the CO/H_2 ratio of 1 and 0.5 can be acquired. During the eCRR, syngas is the main product with a total FE of CO and H_2 of nearly 80%. For the CO/H_2 ratio of 1:2, the ZnLa-1/CN catalyst can reach a current density of 2.5 mA/cm^2, with a CO FE of 25.99% in 0.1 M $KHCO_3$, higher than many reports. Density functional theory (DFT) calculations have unraveled that different Zn:La ratio is the key factor to modulate the CO/H_2 ratio in the final syngas. Zn sites mainly contribute to the CO_2 adsorptions, while the La sites

[1]Tianjin Key Lab for Rare Earth Materials and Applications, Center for Rare Earth and Inorganic Functional Materials, School of Materials Science and Engineering, National Institute for Advanced Materials, Nankai University, Tianjin 300350, China. [2]Department of Applied Biology and Chemical Technology, The Hong Kong Polytechnic University, Hong Kong SAR, China.
*Corresponding author. Email: bhuang@polyu.edu.hk (B.H.); ypdu@nankai.edu.cn (Y.D.)

promote the formation of H_2. Therefore, this work has indicated a promising design strategy to achieve low-cost and high-efficiency electrocatalysts for the generation of syngas for broad industrial applications.

RESULTS

Synthesis and morphology

In this work, to prepare the dual atomic catalyst, we mixed a few pieces of melamine sponges, a certain amount of urea, and metal nitrates in water with the assistance of ultrasound. After 70 min of string, the sponges were saturated with urea and metal ions. Then, the sponges were rapidly frozen with liquid nitrogen and were freeze dried for 48 hours to remove the moisture completely. The final samples with isolated single Zn and La atoms anchored on thin rolled carbon nitride nanosheets were obtained by further annealing under N_2 atmosphere at 550°C. The annealed samples with a dark yellow color were ground by an agate mortar for further characterization. CO_2 and H_2O were transformed into syngas (CO and H_2) by electrochemical process, as shown in Fig. 1.

To investigate the morphology of the as-prepared dual and single atom catalysts, we carried out scanning electron microscopy (SEM) for all samples. As shown in fig. S1, the four catalysts all show the morphology of thin rolled nanosheets. The transmission electron microscopy (TEM) was carried out to further confirm the morphology of curled nanosheets (fig. S2). The scanning TEM (STEM) images in Fig. 2 (A and D) also prove this. In general, the nanostructures of all catalysts are rolling flakes with very little difference, which shows that the addition of different metals has little effect on the morphology. The energy-dispersive spectroscopy (EDS) mapping was conducted to ascertain the elemental distribution of the samples. The fabricated dual atomic catalyst of ZnLa-1/CN shows a homogeneous distribution of both Zn and La from the elemental mapping images (Fig. 2A). The uniform dispersion of nitrogen and lanthanum on carbon nitride substrate can also be visually observed in the elemental mapping images in Fig. 2D. Single atom catalyst of Zn/CN shows uniform distribution of Zn and N (fig. S3A). Meanwhile, fig. S3B exhibits evenly distributed Zn, La, and N in ZnLa-2/CN. The atomic content of the catalysts was also

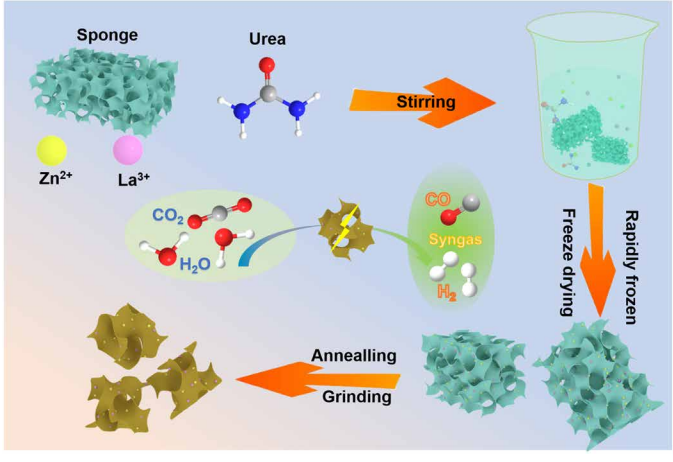

Fig. 1. Schematic illustration of the synthesis process of dual atomic ZnLa catalyst.

preliminarily determined by EDS tests, as shown in fig. S4. Zn or La with 100% content was detected in the catalysts of Zn/CN and La/CN, respectively. As for the dual atomic catalyst of ZnLa-1/CN, Zn with 66.66% atomic percentage and 33.34% of La were probed with an atomic ratio of Zn:La close to 2:1, which is close to the feed ratio. More La species in the catalyst was detected than Zn (38.60% for Zn and 61.40% for La) in the sample of ZnLa-2/CN (Zn:La close to 1:2). The loading contents were further confirmed by inductively coupled plasma optical emission spectrometry, as shown in table S1. It is noted that Zn:La shows a ratio of 2 in ZnLa-1/CN. In ZnLa-2/CN, the La ratios become higher, where La:Zn shows a ratio of 1.6. The aberration-corrected (AC) high-angle annular dark-field STEM (HAADF-STEM) images of ZnLa-1/CN are shown in Fig. 2 (B and C), and no obvious nanoparticles can be found. Meanwhile, isolated bright spots are clearly distinguished from the matrix, indicating atomic dispersion of Zn and La species in ZnLa-1/CN. Figure 2 (E and F) shows AC HAADF-STEM images of La atomic catalysts. The bright dots (highlighted by yellow circles) can be obviously observed, which corresponds to monodispersed single La atoms on CN substrate.

Structure analysis

To further characterize the dual atomic catalyst, the x-ray absorption near-edge structure spectroscopy (XANES) has been carried out to explore the chemical states and coordinated environments of the ZnLa-1/CN. As shown in Fig. 3A, the Zn K-edge spectra of ZnLa-1/CN have been compared with Zn foil and ZnO. For the atomic Zn sites, the line intensity peak is located between Zn foil and ZnO, which indicates the positive charge of the Zn. This is attributed to strong interactions with the CN substrate. The Fourier transform (FT) extended x-ray absorption fine structure (EXAFS) spectra of the ZnLa-1/CN only show one peak near 1.53 Å, which can be assigned to Zn-N bondings (Fig. 3B). Because of the absence of Zn-Zn bondings, the atomic dispersion of Zn sites is fully confirmed. Similarly, the La L3-edge XANES spectra of ZnLa-1/CN have verified that the valence states of La sites are smaller than +3 of La_2O_3 (Fig. 3C). Compared to Zn, La atoms have exhibited both La-C and La-N bondings, supporting the strong interactions with the substrate (Fig. 3D). In addition, the EXAFS data fitting results of ZnLa-1/CN are also displayed in table S2, where the Zn-N shows a lower coordination number of 2.6 at a distance of 1.98 Å, while La-N shows a higher coordination number of 6 at a distance of 2.28 Å. Moreover, the La-C also displays a higher coordination number of 10 at a distance of 3.29 Å. Therefore, the EXAFS data have fully confirmed the local coordination environments of ZnLa-1/CN, where the atomic dispersion of dual metal Zn and La is demonstrated clearly.

Electrochemical analysis

The electrocatalytic CO_2 reduction performances were evaluated through a standard three-electrode system in 0.1 M $KHCO_3$ at room temperature. Figure 4A displays the FE of both CO and H_2 at the potential of −1.5 V versus reversible hydrogen electrode (RHE) for all four catalysts. As shown in the diagram, with the increasing of amount of La species, the FE of CO gradually declines, successfully achieving proportional regulation of syngas. According to the results, we can conclude that the Zn species is responsible for CO production rather than La for H_2. Although the FE of CO and H_2 are changing, the total FE of the gas product shows almost no

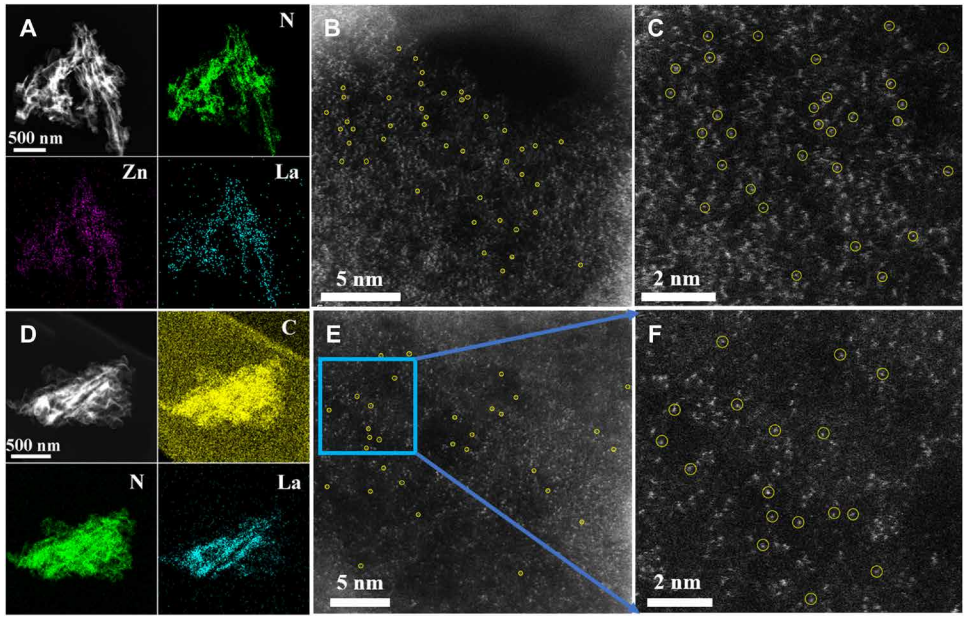

Fig. 2. Elemental distribution and structure characterizations of dual atomic catalyst of ZnLa-1/CN and single atom catalyst of La/CN. (**A**) Elemental mapping of the catalyst of ZnLa-1/CN. (**B** and **C**) AC HAADF-STEM images of dual atomic catalyst of ZnLa-1/CN. (**D**) Elemental mapping of single atom catalyst of La/CN. (**E**) AC HAADF-STEM image of catalyst of La/CN. (**F**) Enlarged image in the blue rectangle area of Fig. 1E.

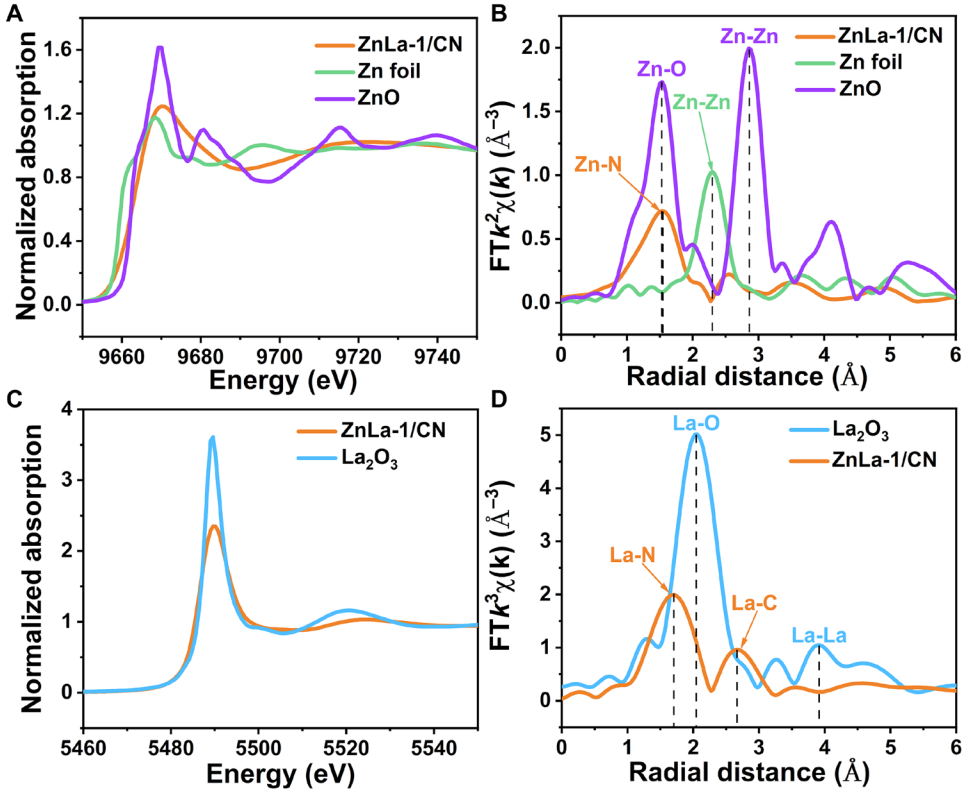

Fig. 3. Atomic structural analysis of the ZnLa-1/CN catalysts. (**A**) Zn K-edge XANES spectra of ZnLa-1/CN, Zn foil, and ZnO. (**B**) Fourier transform (FT) EXAFS spectra for the Zn K-edge. (**C**) La L3-edge XANES spectra of ZnLa-1/CN and La_2O_3. (**D**) FT spectra from EXAFS for La_2O_3 and ZnLa-1/CN in R space.

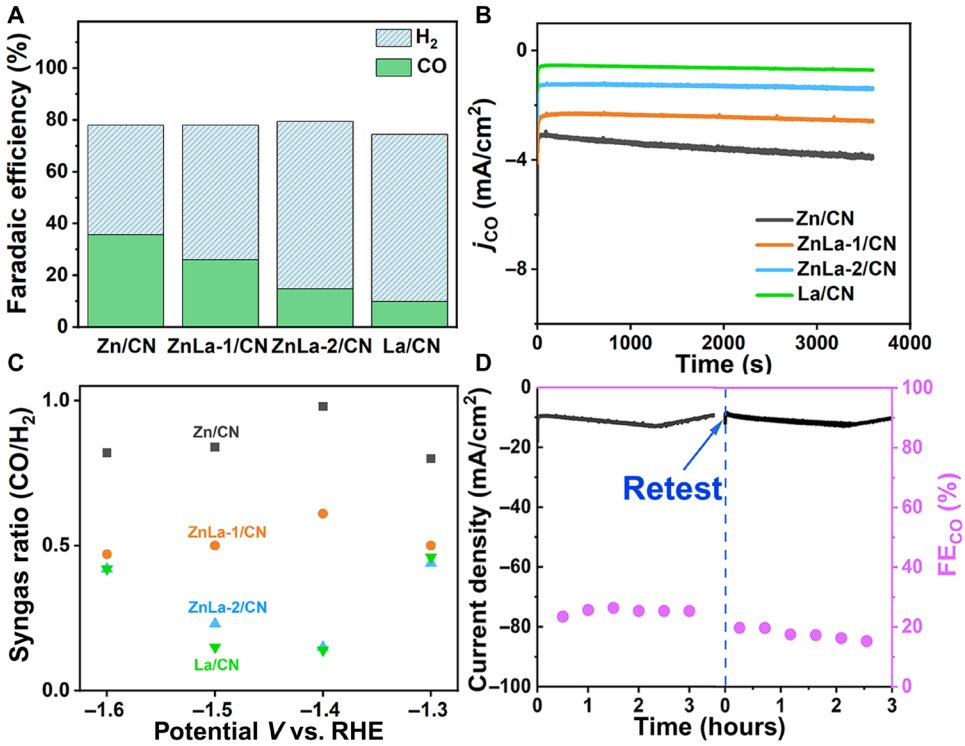

Fig. 4. Catalytic performance of electrocatalytic reduction of CO_2 to syngas. (**A**) FE of different catalysts at −1.5 V versus RHE. (**B**) Corresponding current densities of catalysts at the potential of −1.5 V versus RHE. (**C**) The ratio of CO/H_2 for different catalysts at the potential range of −1.3 to −1.6 V versus RHE. (**D**) Stability test of ZnLa-1 at −1.5 V versus RHE.

change, maintaining 80% of total current density, which means the FE of syngas is about 80%. Specifically, the FE of CO and H_2 are almost equal to 1 for Zn/CN at −1.5 V versus RHE, which is near to the syngas ratio for dimethyl ether synthesis. It is worth noting that for ZnLa-1/CN, the FE of H_2 is exactly twice of CO, meaning the amount ratio of $CO/H_2 = 0.5$, which is similar to the range of syngas compositions for methanol synthesis and Fischer-Tropsch reactions. The corresponding current density of CO is shown in Fig. 4B, which agrees with the results in Fig. 4A, more La content and lower CO current density. The total current densities are also displayed in fig. S5, showing the same trend as Fig. 4B. As shown in Fig. 4C, all catalysts exhibit voltage-dependent behavior. Also, with the increase in La content, the FE of hydrogen increases at any voltage listed. Notably, the catalyst of ZnLa-1/CN produced syngas with a ratio of 0.5 over a relatively wide range of voltage. The stability was also evaluated by conducting a long time current density vs time (I-t) test for ZnLa-1/CN at −1.5 V versus RHE (Fig. 4D). After 3 hours of electrocatalytic process, there was almost no change in the current density of ZnLa-1/CN. The FE of CO only shows a minor change. Meanwhile, after drying in vacuum, both the current density and FE of CO have recovered to the original level of the catalysts. For comparison, the Zn powder, Pt/C, and CN were tested under the same condition (figs. S6 and S7), which shows much lower FE of syngas than the synthesized samples. These results confirm the modulatable ratio between CO and H_2 based on the synthesized dual metal atomic catalysts for further industrial applications. The sample after the stability test was also characterized. As shown in fig. S8, isolated metal atoms can be distinguished from the substrate. Zn and La still evenly distributed in the CN after stability test (fig. S8, B to D). The EDS results reveal Zn and La with certain ratio can also be detected (fig. S9).

Meanwhile, to verify the interactions between the isolated Ln and Zn atoms, we also tested the electrochemical performances of the mixed samples with certain ratios of Zn/CN and La/CN, which show totally different and poor reactivity compared with ZnLa-1/CN and ZnLa-2/CN (fig. S10). These results confirm that the Zn and La sites are not completely isolated to each other, where the interactions between these metal sites achieve the modulations of H_2 and CO ratios in the syngas. The liquid products were characterized by ^1H nuclear magnetic resonance (NMR). For all samples, there is only formic acid or ethanol that can be detected in the electrolyte (fig. S11). The FE of CO and the corresponding current density of CO at the CO/H_2 ratio of 0.5 were compared with the catalysts reported (table S3). The dual atomic catalyst of ZnLa-1/CN shows a relatively high FE_{CO} of 25.99% with j_{CO} of 2.5 mA/cm^2, surpassing many reported catalysts.

The x-ray diffraction (XRD) patterns of La/CN, ZnLa-2/CN, ZnLa-1/CN, and Zn/CN atomic catalysts are shown in Fig. 5A, the only broader diffraction peak at about 26° indexed to the stacking of the conjugated aromatic system of nitrogen-doped carbon. Also, no peaks corresponding to metallic Zn or La are detected, suggesting that the highly dispersed Zn or La species in the single or dual atomic catalysts agree with the results of the AC HAADF-STEM images. The XRD pattern of the sample without any metal elements is also shown in fig. S12, and the only peak of nitrogen-doped carbon was detected similarly. The dual atomic catalyst of ZnLa-2/CN and

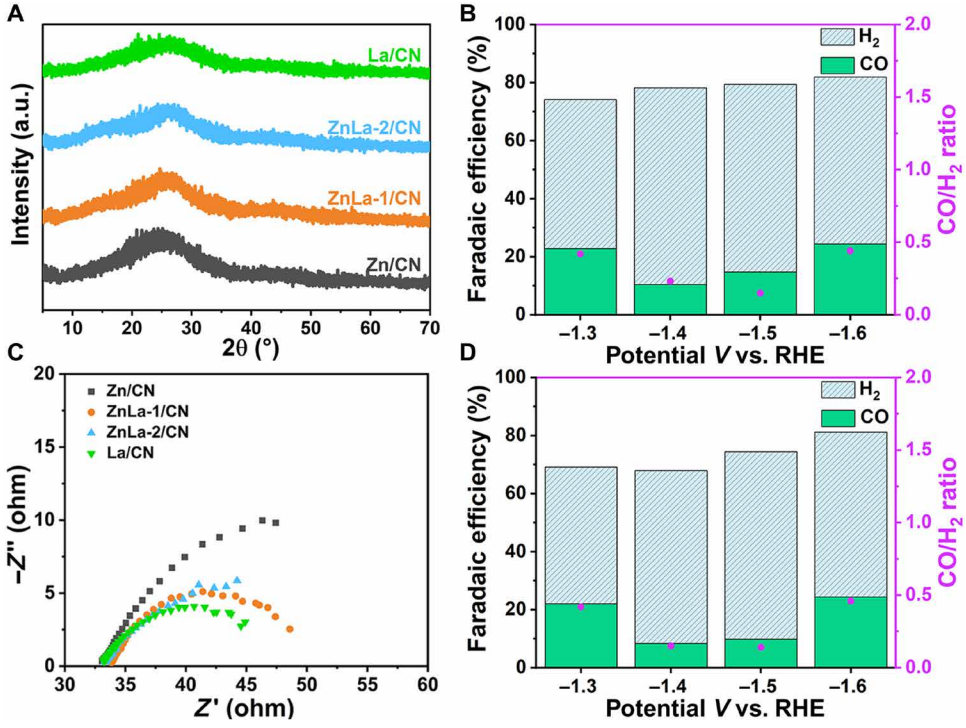

Fig. 5. XRD patterns and catalytic performance of catalysts. (**A**) XRD patterns of the samples. (**B**) The FE and corresponding syngas ratio of ZnLa-2/CN. (**C**) The EIS curves of Zn/CN, ZnLa-1/CN, ZnLa-2/CN, and La/CN. (**D**) The FE and corresponding syngas ratio of La/CN. a.u., arbitrary unit.

single atom catalyst of La/CN also exhibit potential dependence on performance at the potential range of −1.3 to −1.6 V. Figure 5 (B and D) shows the FE of CO and H_2 of ZnLa-2/CN and La, and the corresponding ratio of CO/H_2 is also calculated. At the potential of −1.3 and −1.6 V, CO/H_2 ratio slightly lower than 0.5 was acquired. However, at the potential of 1.4 and − 1.5 V, a larger proportion of H_2 are obtained. A range of CO/H_2 ratios of 0.15 to 0.14 for ZnLa-2/CN and 0.14 to 0.46 for La/CN are acquired, respectively. Meanwhile, the FE of Zn/CN and ZnLa-1/CN are displayed in fig. S13, where the CO generation has been substantially suppressed in ZnLa-1/CN, while the FE of H_2 has been significantly improved. The FE of the H_2/CO ratio is around 2 in ZnLa-1/CN. The electrochemical impedance spectroscopy (EIS) measurements were carried out for the electrodes. As shown in Fig. 5C and fitted curves showed in fig. S14, all the samples show nearly same *R*s. The charge-transfer resistance (R_{ct}) of La/CN is the smallest. ZnLa-1/CN and ZnLa-2/CN showed similar R_{ct}, which are much smaller than that of Zn/CN. In general, by adjusting the ratio of the single atom site in Zn and La atomic catalysts, the syngas with different CO/H_2 ratios can be obtained.

Valence state analysis

As shown in Fig. 6, surface chemical states of La and Zn in different samples and La_2O_3, ZnO were tested and compared. The x-ray photoelectron spectroscopy (XPS) spectra of La 3d and Zn 2p and corresponding spectra of La_2O_3 and ZnO are shown in Fig. 6 (A and B). The peaks of La 3d of ZnLa-1 are shifted toward high binding energy compared with that of La_2O_3 in Fig. 6A, and the peaks of Zn 2p also show the same tendency compared with that of ZnO in Fig. 6B, proving that strong interactions exist between the surface metal and the substrate CN. These results also indicate that La and Zn atom orbitals have been changed by N atoms; reforming of the electronic structure of La and Zn may occur in the CN substrate (*28*). The results of the La XPS spectra reveal that the oxidation states of La species in ZnLa-1/CN are both located between that of La^0 and La^{3+} (*23*), which is caused by the interaction of La and coordinated N from CN. The XPS spectra of La 3d and Zn 2p of ZnLa-1/CN (Fig. 6, C and D) also appear different with single atom catalysts of La/CN and Zn/CN, respectively, indicating that there are interactions between the isolated La and Zn atoms, which is consistent with the results of the experiments (*28*).

DFT calculations

To unravel the electronic change induced by the anchoring of Zn and La, we have further carried out the theoretical explorations through DFT calculations. With the introduction of Zn and La dispersed atoms, the electronic distributions have been evidently modulated (Fig. 7A). For ZnLa-1/CN, the bonding orbitals near the Fermi level (E_F) are mainly contributed by the N-doped amorphous carbon substrate. Meanwhile, the antibonding orbitals show contributions from Zn and amorphous carbon, showing a strong orbital coupling. For ZnLa-2/CN, we notice that Zn and La sites contribute to the bonding and antibonding orbitals, respectively (Fig. 7B). The amorphous carbon supplies a highly electroactive substrate to support the efficient site-to-site electron transfer. The amorphous structure of N-doped carbon has supplied flexible anchoring sites for both Zn and La atoms, where no evident distortions are caused by the introduction of single metal atoms on the surface (Fig. 7, C and D). Then, we further investigate the projected partial density of states (PDOS) of both ZnLa-1 and ZnLa-2 (Fig. 7, E and F).

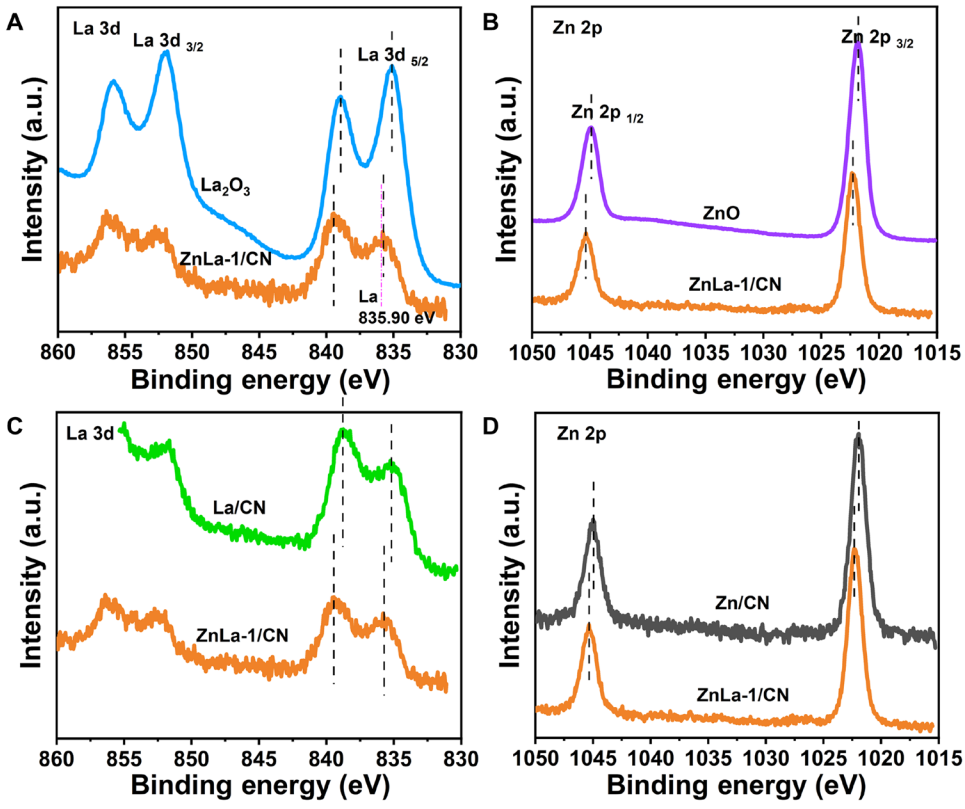

Fig. 6. XPS spectra of Zn 2p and La 3d of catalysts. (**A**) La 3d spectra of ZnLa-1/CN and La_2O_3. (**B**) Zn 2p spectra of the catalyst of ZnLa-1/CN and ZnO. (**C**) La 3d spectra of the dual atomic catalyst of ZnLa-1/CN and the single atom catalyst of La/CN. (**D**) Zn 2p spectra of both catalysts of ZnLa-1/CN and Zn/CN.

For ZnLa-1/CN, Zn 3d is located in a deep position at E_V −7.18 eV, indicating the electron reservoir for stable adsorption of CO_2. Both the s and p orbitals of N-doped carbon and La 5d orbitals contribute to the electron density near E_F. Meanwhile, the conduction band minimum is mainly dominated by La 5d orbitals. Notably, Zn 4s only slightly contributes to electroactivity. With the decrease in the Zn:La ratio in ZnLa-2/CN, the electronic structures of Zn 3d do not show any evident change. La 5d orbitals have downshifted slightly toward E_F with increased electron density, facilitating the electron transfer for the generation of H_2. From the site-dependent PDOS of N-doped carbon, it is noted that low coordinated C and N sites demonstrate the high electroactivity due to the significantly increased electron density near E_F (Fig. 7G). Therefore, the amorphous N-doped carbon with abundant low coordinated sites not only supplies flexible sites for single metal atoms but also guarantees efficient site-to-site electron transfer. On the basis of the electronic structures, ZnLa dual metal atomic catalysts have shown modulatable electronic structures based on the metal ratios. During the electrocatalysis, La and Zn sites are responsible for the generation of H_2 and CO, respectively. The highly electron-rich N-doped carbon effectively promotes the site-to-site electron transfer in the structures. To verify this, we have further compared the adsorption energies of key reactants and products including CO_2, CO, H, and H_2 on different sites (Fig. 7H). For both CO_2 and CO, most sites show the energetically favored adsorptions, in which the Zn sites have shown a particularly strong preference over other sites. Meanwhile, the H adsorptions are much more preferred on La sites to further form the H_2. All different sites have shown a similar trend for the adsorption of H_2, where the relatively weak adsorption suppresses the overbinding effect. Then, we further compared the free energy change for the generation of CO in both ZnLa-1/CN and ZnLa-2/CN (Fig. 7I). The initial adsorption of CO_2 on ZnLa-1/CN and ZnLa-2/CN shows a distinct reaction trend, where ZnLa-2/CN shows an energy barrier of 0.58 eV, while ZnLa-1/CN shows the spontaneous reaction trend. The following hydrogenation to form COOH* shows a downhill trend on both catalyst surfaces. For the desorption of formed CO, ZnLa-1/CN and ZnLa-2/CN exhibit energy barriers of 0.32 and 0.13 eV. Moreover, for the reduction of CO_2, ZnLa-1/CN shows the exothermic reaction with an energy release of 0.94 eV. In comparison, ZnLa-2/CN requires an energy cost of 0.72 eV for the CO_2 reduction, supporting the low CO concentration in the syngas. For the formation of H_2, both ZnLa-1/CN and ZnLa-2/CN show an exothermic reaction trend with an energy release of 1.34 and 2.01 eV (Fig. 7J). Moreover, the suppression of overbinding effect facilitates the desorption of formed H_2 on ZnLa-1/CN and ZnLa-2/CN, which only costs 0.09 and 0.05 eV, guaranteeing efficient H_2 generation. The much stronger energy trend of H_2 generation than the formation of CO determines the dominant contribution of the H_2 in the syngas, which is consistent with the experiments.

DISCUSSION

In conclusion, a series of single and dual atomic catalysts were obtained through impregnation and annealing according to the AC

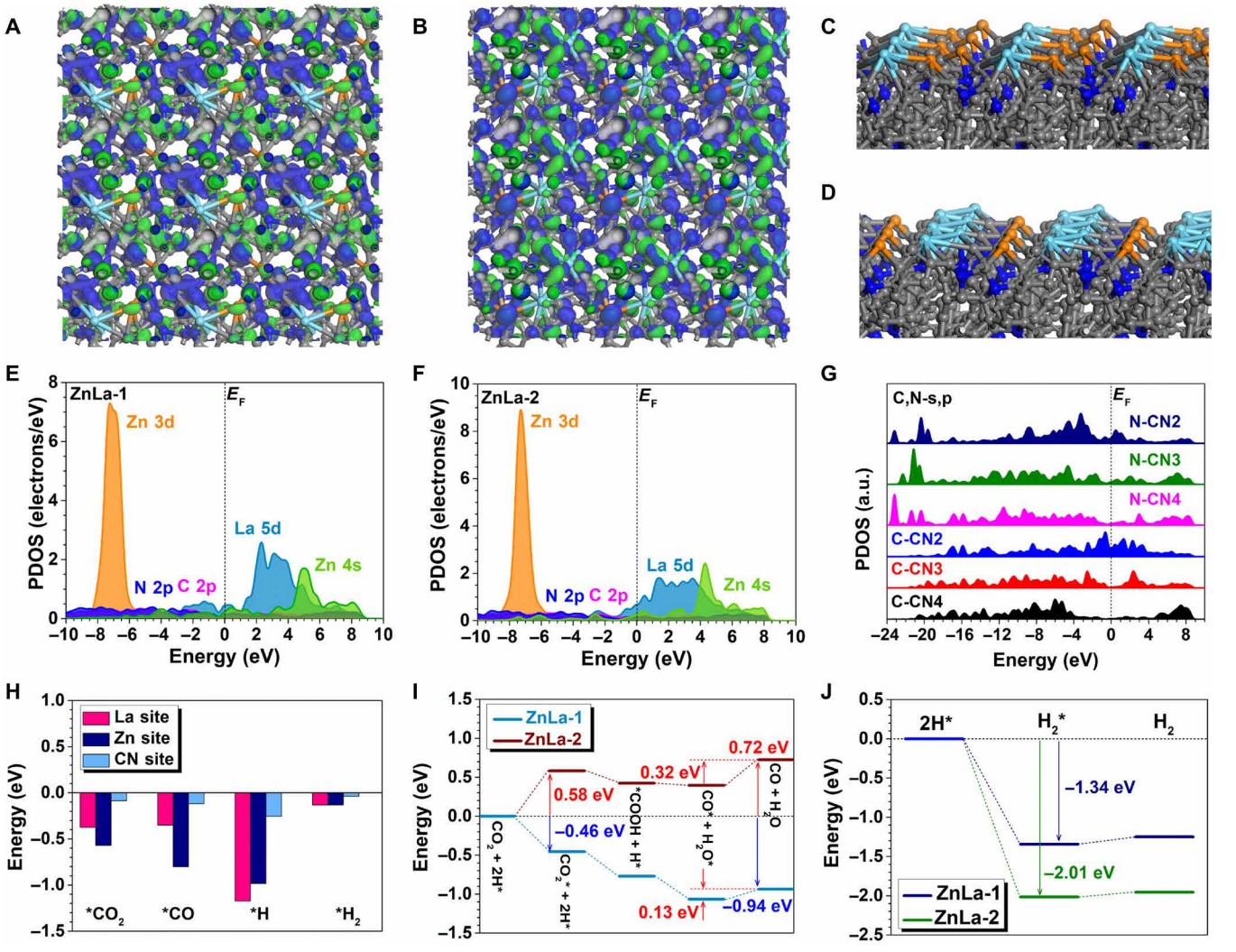

Fig. 7. Theoretical calculations of ZnLa dual atomic catalysts. The three-dimensional contour plot of electronic distributions of (**A**) ZnLa-1/CN and (**B**) ZnLa-2/CN. Gray balls, C; blue balls, N; orange balls, Zn; and light blue balls, La. Blue isosurface, bonding orbitals; green isosurface, antibonding orbitals. The side view for relaxed structures of (**C**) ZnLa-1/CN and (**D**) ZnLa-2/CN. PDOS of (**E**) ZnLa-1/CN and (**F**) ZnLa-2/CN. (**G**) Site-dependent PDOS of C and N sites. CN, coordination number. (**H**) Adsorption energy costs of key reactants and products on different sites. (**I**) Energy profile for the formation of CO and H_2O. (**J**) Energy profile for the formation of H_2.

HAADF-STEM images. Syngas with different ratio of CO/H_2 can be obtained by adjusting the single atom sites of Zn and La. Notably, the dual atomic catalyst of ZnLa-1/CN produces syngas with a ratio of CO/H_2 = 0.5 at a wide potential range of −1.6 to 1.3 V, which is favorable for methanol synthesis and Fischer-Tropsch reactions. Meanwhile, at the potential of −1.5 V, the FE_{CO} of ZnLa-1/CN can reach 25.99% with a current density of CO of 2.5 mA/cm^2, and FE_{CO} remains almost unchanged after a long time of electrochemical reaction. The single atom sites of Zn and La prefer to generate CO and H_2, respectively, according to the results of electrochemical tests. DFT calculations have investigated the modulations of electronic structure induced by the anchoring of Zn and La atoms. The electron-rich feature of ZnLa-1/CN guarantees not only the strong electron transfer but also the high FE for the syngas. This work shows that RE elements can be combined with other transition metal elements to produce syngas through electrocatalytic CO_2 reduction, providing a new solution for the high-value utilization of RE elements.

MATERIALS AND METHODS

Chemicals

The chemicals used were $Zn(NO_3)_2{\cdot}6H_2O$ [Analytical Reagent (AR), Aladdin], $La(NO_3)_3{\cdot}6H_2O$ (AR, Aladdin), and urea [American Chemical Society (ACS), Aladdin). Ultrapure water (18.2 megohms·cm) was used as solvent. Carbon papers (TGP-H-0600) were purchased from Toray Industries Inc.

Synthesis of ZnLa-1/CN atomic catalysts

The single and dual atomic catalysts in this research were fabricated according to a previous report (*23*). In detail, for the synthesis of ZnLa-1/CN, 21.6 g of urea was dissolved in a 20-ml ultrapure water with ultrasonic assistance. Then, 0.64 mmol $Zn(NO_3)_2{\cdot}H_2O$ and 0.32 mmol $La(NO_3)_3{\cdot}H_2O$ were dissolved in the urea aqueous solution to form a transparent solution. A few pieces of melamine sponges were then soaked in the solution and stirred at room temperature for 70 min. Last, the sponges filled with the mixture solution of urea

and metallic nitrate were immediately frozen in liquid nitrogen and then dried in a vacuum freeze dryer for at least 48 hours. The final catalyst was obtained by annealing the above sponges in a tube furnace at 550°C for 4 hours under the N_2 atmosphere with a heating rate of 5°C/min. The annealed sponges were ground into powders for further tests.

Synthesis of samples of Zn/CN, ZnLa-2/CN, and La/CN atomic catalysts

The procedures of the synthesis of the catalysts of Zn/CN, ZnLa-2/CN, and La/CN were similar to that of ZnLa-1/CN. Only $Zn(NO_3)_2{\cdot}H_2O$ or $La(NO_3)_3{\cdot}H_2O$ was added respectively for the synthesis of Zn and La. $Zn(NO_3)_3{\cdot}H_2O$ (0.32 mmol) and $La(NO_3)_3{\cdot}H_2O$ (0.64 mmol) were used in the synthesis of ZnLa-2. The molar amount of total metal nitrate was controlled equally.

Structure and property

The morphologies of the samples were characterized by TEM and high-resolution TEM on a JEM-2800 microscope (JEOL, Japan), operating at an acceleration voltage of 200 kV. Field emission SEM images were obtained on a JSM-7800F microscope (JEOL, Japan), operating at an acceleration voltage of 0.01 to 30 kV. The crystalline structures of the as-obtained samples were tested by XRD on a Rigaku SmartLab XRD (Rigaku, Japan) with Cu Kα radiation (λ = 1.5406 Å, 20 mA, and 40 kV). XPS was performed using an ESCALAB 250Xi spectrometer using a monochromatic Al Kα x-ray source ($h\upsilon$ = 1486.6 eV) as the excitation source (Thermo Fischer Scientific, USA). HAADF-STEM images were obtained at 300 kV with an FEI Titan Cubed Themis G2 300. The x-ray absorption spectra, including XANES and EXAFS, of the samples at Co K-edge (7709 eV) were collected at the Singapore Synchrotron Light Source center, where a pair of channel-cut Si (111) crystals was used in the monochromator. The Co K-edge XANES data were recorded in a transmission mode. Co foil CoO and CoO were used as references. The storage ring was working at the energy of 2.5 GeV with an average electron current of below 200 mA. The acquired EXAFS data were extracted and processed according to the standard procedures using the ATHENA module implemented in the FEFIT software packages. The k3-weighted FT of $x(k)$ in R space was obtained over the range of 0 to 14.0 Å by applying a Besse window function.

Electrochemical tests

The electrochemical tests were carried out with a standard three-electrode system at an electrochemical workstation (CHI660E). The dispersions of catalysts for further electrochemical tests were prepared by dispersing 5 mg of catalyst and 2 mg of conductive carbon black into 500 μl of solution containing isopropyl alcohol and water (the volume ratio of alcohol and water is 1:1) and 20 μl of Nafion. The final inks were obtained by ultrasound treat of the dispersions for at least 30 min. The electrodes were prepared by coating 20 μl of obtained inks in a 1 cm × 1 cm area in carbon papers with sizes of 1 cm × 2 cm and dried in air. Electrochemical CO_2 reduction was conducted using a three-electrode configuration in a CO_2 saturated 0.1 M $KHCO_3$ (pH 6.8) solution using an H cell with compartments separated by an ion exchange membrane (Nafion117). An Ag/AgCl electrode and a Pt electrode were applied as a reference and counter electrodes, respectively. Carbon papers coated with catalysts were used as cathodes. Before a long-time I-t test, several Cyclic Voltammetry (CV) tests were conducted to acquire a stable state. All potentials were transformed to the RHE reference by using the formula $E_{RHE} = E_{Ag/AgCl} + 0.059 \times pH$. During the electrochemical process, CO_2 was bubbled in the electrolyte with a rate of 20 sccm for at least 30 min to maintain the saturation of CO_2. EIS was measured at a potential of −1.5 V versus RHE from 0.01 Hz to 100 kHz, with an amplitude of 10 mV in Autolab PGSTAT302N.

Product analysis

To determine the products and their FE, electrolysis was carried out at the selected potential for 60 min. Gaseous products in the cathodic compartment were periodically vented into the gas sampling loop of a gas chromatograph (GC; 2014c). The concentration of gaseous products was quantified by on-line GC. The FE of CO and H_2 were calculated by the following equation

$$\mathrm{FE} = \frac{nvPf_vF}{RTI} \times 100\%$$

where n is the number of electrons transferred to form the target product (n is 2 when the product is CO or CHOOH); v is the volume fraction of target product in the exhaust gases, which is equal to mole fraction when the gases are considered as ideal gas; F is Faraday's constant (96,485 C mol^{-1}); f_v represents the volume flow rate of exhaust gases, which is measured at room temperature (T) and under ambient pressure (p) by a flow meter; and I is the steady-state current. The liquid products were collected after 1 hour of electrolysis quantitatively analyzed using 400 MHz ^{1}H NMR spectroscopy (Bruker AVANCE NEO 600 MHz). In detail, 400 μl of electrolyte mixed with 50 μl of dimethyl sulfoxide (20 mM) and 100 μl of D_2O was used as the internal standard.

Calculation setup

To investigate the electronic structure, we have selected DFT calculations within CASTEP packages for different ratio of Zn:La in the atomic catalyst (*39*). To deal with the exchange correlation energy, we chose the generalized gradient approximation and Perdew-Burke-Ernzerhof in this work (*40*–*42*). We have set the plane wave basis cutoff energy to 380 eV by considering the ultrafine quality. The ultrasoft pseudopotentials with the Broyden-Fletcher-Goldfarb-Shanno algorithm are applied for all the geometry optimizations. Meanwhile, the coarse quality of the k-point set was used for the energy minimizations to guarantee both accuracy and efficiency of calculations *(43)*. To guarantee full relaxations for all the structure and adsorption of intermediates, we have applied 20-Å vacuum space in the z axis for sufficient space. Meanwhile, the convergence criteria of the geometry optimizations have been set as follows: The Hellmann-Feynman forces on the atom should be less than 0.001 eV/Å; the total energy difference and the interionic displacement should be less than 5×10^{-5} eV per atom and 0.005 Å, respectively.

SUPPLEMENTARY MATERIALS

Supplementary material for this article is available at https://science.org/doi/10.1126/sciadv.abl4915

REFERENCES AND NOTES

1. S. Chen, Y. Su, P. Deng, R. Qi, J. Zhu, J. Chen, Z. Wang, L. Zhou, X. Guo, B. Y. Xia, Highly selective carbon dioxide electroreduction on structure-evolved copper perovskite oxide toward methane production. *ACS Catal.* **10**, 4640–4646 (2020).

2. K. Fan, Y. Jia, Y. Ji, P. Kuang, B. Zhu, X. Liu, J. Yu, Curved surface boosts electrochemical CO_2 reduction to formate via bismuth nanotubes in a wide potential window. *ACS Catal.* **10**, 358–364 (2019).
3. D. Gao, H. Zhou, J. Wang, S. Miao, F. Yang, G. Wang, J. Wang, X. Bao, Size-dependent electrocatalytic reduction of CO_2 over Pd nanoparticles. *J. Am. Chem. Soc.* **137**, 4288–4291 (2015).
4. Y. Gao, F. Li, P. Zhou, Z. Wang, Z. Zheng, P. Wang, Y. Liu, Y. Dai, M.-H. Whangbo, B. Huang, Enhanced selectivity and activity for electrocatalytic reduction of CO_2 to CO on an anodized Zn/carbon/Ag electrode. *J. Mater. Chem. A* **7**, 16685–16689 (2019).
5. Y. Gao, Q. Wu, X. Liang, Z. Wang, Z. Zheng, P. Wang, Y. Liu, Y. Dai, M. H. Whangbo, B. Huang, Cu_2O Nanoparticles with both {100} and {111} facets for enhancing the selectivity and activity of CO_2 electroreduction to ethylene. *Adv. Sci.* **7**, 1902820 (2020).
6. M. He, C. Li, H. Zhang, X. Chang, J. G. Chen, W. A. Goddard 3rd, M. J. Cheng, B. Xu, Q. Lu, Oxygen induced promotion of electrochemical reduction of CO_2 via co-electrolysis. *Nat. Commun.* **11**, 3844 (2020).
7. Q. Hu, Z. Han, X. Wang, G. Li, Z. Wang, X. Huang, H. Yang, X. Ren, Q. Zhang, J. Liu, C. He, Facile synthesis of sub-nanometric copper clusters by double confinement enables selective reduction of carbon dioxide to methane. *Angew. Chem. Int. Ed.* **59**, 19054–19059 (2020).
8. Z. Jiang, T. Wang, J. Pei, H. Shang, D. Zhou, H. Li, J. Dong, Y. Wang, R. Cao, Z. Zhuang, W. Chen, D. Wang, J. Zhang, Y. Li, Discovery of main group single $Sb–N_4$ active sites for CO_2 electroreduction to formate with high efficiency. *Energy Environ. Sci.* **13**, 2856–2863 (2020).
9. L. Jiao, W. Yang, G. Wan, R. Zhang, X. Zheng, H. Zhou, S. H. Yu, H. L. Jiang, Single-atom electrocatalysts from multivariate metal-organic frameworks for highly selective reduction of CO_2 at low pressures. *Angew. Chem. Int. Ed.* **59**, 20589–20595 (2020).
10. M. G. Kibria, J. P. Edwards, C. M. Gabardo, C. T. Dinh, A. Seifitokaldani, D. Sinton, E. H. Sargent, Electrochemical CO_2 reduction into chemical feedstocks: From mechanistic electrocatalysis models to system design. *Adv. Mater.* **31**, e1807166 (2019).
11. M. Li, B. Hua, L.-C. Wang, J. D. Sugar, W. Wu, Y. Ding, J. Li, D. Ding, Switching of metal–oxygen hybridization for selective CO2 electrohydrogenation under mild temperature and pressure. *Nat. Catal.* **4**, 274–283 (2021).
12. N. Han, P. Ding, L. He, Y. Li, Y. Li, Promises of main group metal–based nanostructured materials for electrochemical CO_2 reduction to formate. *Adv. Energy Mater.* **10**, 1902338 (2020).
13. Q. Chang, J. Kim, J. H. Lee, S. Kattel, J. G. Chen, S. I. Choi, Z. Chen, Boosting activity and selectivity of CO_2 electroreduction by pre-hydridizing Pd nanocubes. *Small* **16**, e2005305 (2020).
14. P. Chen, Y. Jiao, Y.-H. Zhu, S.-M. Chen, L. Song, M. Jaroniec, Y. Zheng, S.-Z. Qiao, Syngas production from electrocatalytic CO_2 reduction with high energetic efficiency and current density. *J. Mater. Chem. A* **7**, 7675–7682 (2019).
15. S. Guo, S. Zhao, X. Wu, H. Li, Y. Zhou, C. Zhu, N. Yang, X. Jiang, J. Gao, L. Bai, Y. Liu, Y. Lifshitz, S. T. Lee, Z. Kang, A Co_3O_4-CDots-C_3N_4 three component electrocatalyst design concept for efficient and tunable CO_2 reduction to syngas. *Nat. Commun.* **8**, 1828 (2017).
16. Z. B. Hoffman, T. S. Gray, K. B. Moraveck, T. B. Gunnoe, G. Zangari, Electrochemical reduction of carbon dioxide to syngas and formate at dendritic copper–indium electrocatalysts. *ACS Catal.* **7**, 5381–5390 (2017).
17. S. Min, X. Yang, A.-Y. Lu, C.-C. Tseng, M. N. Hedhili, L.-J. Li, K.-W. Huang, Low overpotential and high current CO_2 reduction with surface reconstructed Cu foam electrodes. *Nano Energy* **27**, 121–129 (2016).
18. R. Daiyan, R. Chen, P. Kumar, N. M. Bedford, J. Qu, J. M. Cairney, X. Lu, R. Amal, Tunable syngas production through CO_2 electroreduction on cobalt-carbon composite electrocatalyst. *ACS Appl. Mater. Interfaces* **12**, 9307–9315 (2020).
19. M. B. Ross, C. T. Dinh, Y. Li, D. Kim, P. De Luna, E. H. Sargent, P. Yang, Tunable Cu enrichment enables designer syngas electrosynthesis from CO_2. *J. Am. Chem. Soc.* **139**, 9359–9363 (2017).
20. W. Sheng, S. Kattel, S. Yao, B. Yan, Z. Liang, C. J. Hawxhurst, Q. Wu, J. G. Chen, Electrochemical reduction of CO_2 to synthesis gas with controlled CO/H_2 ratios. *Energy Environ. Sci.* **10**, 1180–1185 (2017).
21. A. Bagger, W. Ju, A. S. Varela, P. Strasser, J. Rossmeisl, Electrochemical CO_2 reduction: A classification problem. *ChemPhysChem* **18**, 3266–3273 (2017).
22. H. Ding, D. Wang, A. Sadat, Z. Li, X. Hu, M. Xu, P. C. de Morais, B. Ge, S. Sun, J. Ge, Y. Chen, Y. Qian, C. Shen, X. Shi, X. Huang, R.-Q. Zhang, H. Bi, Single-atom gadolinium anchored on graphene quantum dots as a magnetic resonance signal amplifier. *ACS Appl. Biol. Mater.* **4**, 2798–2809 (2021).
23. S. Ji, Y. Qu, T. Wang, Y. Chen, G. Wang, X. Li, J. Dong, Q. Chen, W. Zhang, Z. Zhang, S. Liang, R. Yu, Y. Wang, D. Wang, Y. Li, Rare-earth single erbium atoms for enhanced photocatalytic CO_2 reduction. *Angew. Chem. Int. Ed.* **59**, 10651–10657 (2020).
24. J. Liu, X. Kong, L. Zheng, X. Guo, X. Liu, J. Shui, Rare earth single-atom catalysts for nitrogen and carbon dioxide reduction. *ACS Nano* **14**, 1093–1101 (2020).
25. N. Zhang, H. Yan, L. Li, R. Wu, L. Song, G. Zhang, W. Liang, H. He, Use of rare earth elements in single-atom site catalysis: A critical review commemorating the 100th anniversary of the birth of Academician Guangxian Xu. *J. Rare Earths* **39**, 233–242 (2021).
26. M. Zhu, C. Zhao, X. Liu, X. Wang, F. Zhou, J. Wang, Y. Hu, Y. Zhao, T. Yao, L.-M. Yang, Y. Wu, Single atomic cerium sites with a high coordination number for efficient oxygen reduction in proton-exchange membrane fuel cells. *ACS Catal.* **11**, 3923–3929 (2021).
27. B. Chen, T. Wang, S. Zhao, J. Tan, N. Zhao, S. P. Jiang, Q. Zhang, G. Zhou, H. M. Cheng, Efficient reversible conversion between MoS_2 and Mo/Na_2S enabled by graphene-supported single atom catalysts. *Adv. Mater.* **33**, e2007090 (2021).
28. P. Chen, B. Lei, X. Dong, H. Wang, J. Sheng, W. Cui, J. Li, Y. Sun, Z. Wang, F. Dong, Rare-earth single-atom La-N charge-transfer bridge on carbon nitride for highly efficient and selective photocatalytic CO_2 reduction. *ACS Nano* **14**, 15841–15852 (2020).
29. J. Du, G. Wu, K. Liang, J. Yang, Y. Zhang, Y. Lin, X. Zheng, Z. Q. Yu, Y. Wu, X. Hong, Rapid controllable synthesis of atomically dispersed Co on carbon under high voltage within one minute. *Small* **17**, e2007264 (2021).
30. L. Han, S. Song, M. Liu, S. Yao, Z. Liang, H. Cheng, Z. Ren, W. Liu, R. Lin, G. Qi, X. Liu, Q. Wu, J. Luo, H. L. Xin, Stable and efficient single-atom Zn catalyst for CO_2 reduction to CH_4. *J. Am. Chem. Soc.* **142**, 12563–12567 (2020).
31. K. Jiang, S. Siahrostami, T. Zheng, Y. Hu, S. Hwang, E. Stavitski, Y. Peng, J. Dynes, M. Gangisetty, D. Su, K. Attenkofer, H. Wang, Isolated Ni single atoms in graphene nanosheets for high-performance CO2reduction. *Energy Environ. Sci.* **11**, 893–903 (2018).
32. N. Li, X. Song, L. Wang, X. Geng, H. Wang, H. Tang, Z. Bian, Single-atom cobalt catalysts for electrocatalytic hydrodechlorination and oxygen reduction reaction for the degradation of chlorinated organic compounds. *ACS Appl. Mater. Interfaces* **12**, 24019–24029 (2020).
33. S. Tian, B. Wang, W. Gong, Z. He, Q. Xu, W. Chen, Q. Zhang, Y. Zhu, J. Yang, Q. Fu, C. Chen, Y. Bu, L. Gu, X. Sun, H. Zhao, D. Wang, Y. Li, Dual-atom Pt heterogeneous catalyst with excellent catalytic performances for the selective hydrogenation and epoxidation. *Nat. Commun.* **12**, 3181 (2021).
34. J. Xu, S. Lai, D. Qi, M. Hu, X. Peng, Y. Liu, W. Liu, G. Hu, H. Xu, F. Li, C. Li, J. He, L. Zhuo, J. Sun, Y. Qiu, S. Zhang, J. Luo, X. Liu, Atomic Fe-Zn dual-metal sites for high-efficiency pH-universal oxygen reduction catalysis. *Nano Res.* **14**, 1374–1381 (2021).
35. N. Zhang, X. Zhang, Y. Kang, C. Ye, R. Jin, H. Yan, R. Lin, J. Yang, Q. Xu, Y. Wang, Q. Zhang, L. Gu, L. Liu, W. Song, J. Liu, D. Wang, Y. Li, A supported Pd_2 dual-atom site catalyst for efficient electrochemical CO_2 reduction. *Angew. Chem. Int. Ed.* **60**, 13388–13393 (2021).
36. H. Zhang, W. Cheng, D. Luan, X. W. Lou, Atomically dispersed reactive centers for electrocatalytic CO_2 reduction and water splitting. *Angew. Chem. Int. Ed.* **133**, 13285–13304 (2021).
37. H. Zhang, X. F. Lu, Z.-P. Wu, X. W. Lou, Emerging multifunctional single-atom catalysts/nanozymes. *ACS Cent. Sci.* **6**, 1288–1301 (2020).
38. H. Zhang, W. Zhou, T. Chen, B. Y. Guan, Z. Li, X. W. Lou, A modular strategy for decorating isolated cobalt atoms into multichannel carbon matrix for electrocatalytic oxygen reduction. *Energy Environ. Sci.* **11**, 1980–1984 (2018).
39. S. J. Clark, M. D. Segall, C. J. Pickard, P. J. Hasnip, M. J. Probert, K. Refson, M. C. Payne, First principles methods using castep. *Z Kristallogr.* **220**, 567–570 (2005).
40. J. P. Perdew, K. Burke, M. Ernzerhof, Generalized gradient approximation made simple. *Phys. Rev. Lett.* **77**, 3865–3868 (1996).
41. P. J. Hasnip, C. J. Pickard, Electronic energy minimisation with ultrasoft pseudopotentials. *Comput. Phys. Commun.* **174**, 24–29 (2006).
42. J. P. Perdew, J. A. Chevary, S. H. Vosko, K. A. Jackson, M. R. Pederson, D. J. Singh, C. Fiolhais, Atoms, molecules, solids, and surfaces: Applications of the generalized gradient approximation for exchange and correlation. *Phys. Rev. B* **46**, 6671–6687 (1992).
43. J. D. Head, M. C. Zerner, A Broyden-Fletcher-Goldfarb-Shanno optimization procedure for molecular geometries. *Chem. Phys. Lett.* **122**, 264–270 (1985).

Acknowledgments

Funding: We acknowledge the support from the support from the National Natural Science Foundation of China (21971117, 21771156), Functional Research Funds for the Central Universities, Nankai University (63186005), Tianjin Key Lab for Rare Earth Materials and Applications (ZB19500202), the Open Funds (No. RERU2019001) of the State Key Laboratory of Rare Earth Resource Utilization, 111 Project (No. B18030) from China, Beijing-Tianjin-Hebei Collaborative Innovation Project (19YFSLQY00030), the Outstanding Youth Project of Tianjin Natural Science Foundation (20JCJQJC00130), and the Key Project of Tianjin Natural Science Foundation (20JCZDJC00650). **Author contributions:** Y.D. and B.H. proposed the whole research direction and guided the project. Z.L., L.S., and Y.D. designed and carried out all the synthesis, characterizations, and electrochemical measurements. M.S. and B.H. performed the theoretical calculations and analysis. All the authors contributed to the results analysis and manuscript drafting. **Competing interests:** The authors have submitted a Chinese patent application on the disclosed approach for large-scale synthesis of halide materials. The authors declare that they have no other competing interests. **Data and materials availability:** All data needed to evaluate the conclusions in the paper are present in the paper and/or the Supplementary Materials.

Submitted 16 July 2021
Accepted 1 October 2021
Published 19 November 2021
10.1126/sciadv.abl4915